

# Fingering Instability in a Water-Sand Mixture

A. Lange<sup>1</sup>, M. Schröter<sup>2</sup>, M. A. Scherer<sup>2</sup>, A. Engel<sup>1</sup> and I. Rehberg<sup>2</sup>

<sup>1</sup> Institut für Theoretische Physik, Otto-von-Guericke-Universität, Postfach 4120, D-39016 Magdeburg, Germany

<sup>2</sup> Institut für Experimentelle Physik, Otto-von-Guericke-Universität, Postfach 4120, D-39016 Magdeburg, Germany

Received: date / Revised version: date

**Abstract.** The temporal evolution of a water-sand interface driven by gravity is experimentally investigated. By means of a Fourier analysis of the evolving interface the growth rates are determined for the different modes appearing in the developing front. To model the observed behavior we apply the idea of the Rayleigh-Taylor instability for two stratified fluids. Carrying out a linear stability analysis we calculate the growth rates from the corresponding dispersion relations for finite and infinite cell sizes. Based on the theoretical results the viscosity of the suspension is estimated to be approximately 100 times higher than that of pure water, in agreement with other experimental findings.

**PACS.** 47.54.+r Pattern selection – 47.55.Kf Multiphase and particle-laden flows – 68.10.-m Fluid surfaces and fluid-fluid interfaces – 81.05.Rm Granular materials – 83.70.Hq Suspensions

## 1 Introduction

There has been great interest in the behavior of granular materials over the last years (for a review see [1] and references therein). Examples for the surprising behavior of granular matter are two-dimensional localized states, called oscillons [2], in vertically vibrated containers, stratification phenomena observed while pouring granular mixtures onto a pile [3] or singing sand audible in deserts [4].

In contrast to the amount of phenomena one lacks a sound theoretical explanation for the observations. Difficulties arise due to the highly complex, disordered structure formed by the grains and their nonlinear internal friction. Therefore, most theoretical approaches have been done by numerical methods. Molecular-dynamics simulations and cellular automata calculations are frequently applied, for recent reviews see [5]. These methods describe in some detail the interactions between the particular grains [6]. Conclusions on the macroscopic behavior of granular matter are then drawn from the simulations with a great number of particles. Despite the recent progress in computer performance the size of the systems is still too small for a quantitative comparison with real experiments [6, 7].

Hydrodynamic approaches to granular material are few [8, 9, 10, 11] and are associated with restrictions as no interparticle correlations [8], a Gaussian distribution in the velocity of the grains [9] or steady-state properties [11]. Nevertheless, there are striking phenomenological similarities in the observed patterns for pure granular materials and pure fluids. Experiments with an inclined chute

[12, 13] or a vertically vibrated container [14, 15] show the most notable analogy. It is clear that granular media are different from fluids but under certain conditions these differences are *not prevailing*.

The flow of grains embedded in an interstitial fluid is dominated either by the effects of grain inertia or by effects of fluid viscosity. The Bagnold number  $B$  [16] expresses the ratio of collision forces between the grains to viscous forces in the fluid-grain mixture. A small Bagnold number,  $B < 40$ , characterizes the regime of the macroviscous flow. In this regime the viscous interaction with the pure fluid is important. Examples for this type of flow are mud slides and the transport of water-sand mixtures in river beds. At large Bagnold numbers,  $B > 450$ , the flow is called grain-inertia regime where the grain-grain interactions dominate. All flows of grains with air as interstitial fluid fall into the grain-grain regime.

Here, experiments are performed with sand dispersed in water. The occurring shear rates, the mean particle diameters, and the viscosity of water result in a Bagnold number of about 1 [17]. This motivates the idea to consider the water-sand mixture as fluid-like. In the experiments we observe that the initial flat water-sand interface evolves into a finger-like pattern. The measured velocity for the largest finger was typically three times the Stokes velocity of a settling hard sphere. Furthermore, the velocity was nearly independent of the mass of the sand and the diameter of the particles [17]. This independence of particle properties encourages a fluid-like description of the water-sand mixture. To model this behavior we test a continuum approach which is based on a well-known hydrodynamic instability.

Send offprint requests to: A. Lange

Correspondence to: A. Lange

The aim is to determine the critical parameters for the stability of the pattern and the dispersion relation for the *whole* spectrum of wave numbers detectable in the experiment. Particularly, the latter extends significantly the objectives of earlier experiments with water and polystyrene spheres [18] and with water and glass beads [19]. The dependence of the initial wavelength of the developing pattern on the width of the cell was studied in [18]. In [19] the experiments were focused on the evolution of voidage shock fronts caused by a step increase or decrease in the fluidization velocity for a fluidized bed. We, however, turn our attention to the temporal evolution of *all* wave numbers.

To model the water-sand mixture as a Newtonian fluid with effective properties depending on the concentration of the particles is obviously a simplifying description. In such a model it is assumed that the particle concentration in the flowing mixture is almost constant. Furthermore, the particles have to be large enough to neglect their Brownian diffusion. Stability analyses with these simplifications were made for moderate concentrated mixtures in horizontal Hagen-Poiseuille flow [20] and in sedimentation problems in inclined narrow channels [21, 22, 23]. For the latter configuration even the sediment was described by such a simple model and a fair agreement with experimental results was found [22]. In the clear knowledge of the limitations of a fluid model for the water-sand mixture we will examine whether such an approach can catch the essence of the experimental results.

In the following section, the experimental arrangement is described and the results for the growth rates of the wave numbers are presented. In Sect. 3 the model is explained and thereafter the calculated growth rates are compared with those of the experiment (Sect. 4). The final section contains our conclusions and some remarks about further perspectives.

## 2 Experiment

### 2.1 Experimental setup

A closed Hele-Shaw-like cell is used to investigate the temporal evolution of a water-sand interface driven by gravity (see Fig. 1). The cell, a CCD-camera and a neon tube are fixed to a frame which can be turned around a horizontal axis. This allows image analysis in the comoving frame and ensures a homogeneous illumination at every stage of the pattern forming process. The length of the cell is 160 mm, the height 80 mm and the width 4 mm, respectively. The cell is filled with sand and distilled water. As sand we use spherical glass particles (Würth Ballotini MGL) of different sizes and size distributions (see Table 1 for details). Its material density is given by 2.45 g/cm<sup>3</sup>. The rotation axes of the frame is right beneath the sand layer. This minimizes the centrifugal forces on the sand layer while the cell is turned. The cell is rotated by hand. To obtain reproducible results the vertical and horizontal acceleration is measured by acceleration sensors (ADXL05). When the cell passes a rotation angle of 170 degree, a

lightgate triggers a number of snapshots. This moment defines the starting time of our measurements where we take images every 20 ms for later analysis. The images have a dimension of 256 x 300 pixel. To achieve a reasonable resolution we only focus on a horizontal length of 61 mm at the middle of the cell. This gives a resolution of 4.9 pixel/mm. After each rotation the suspension sediments until all particles are settled. This process takes typically less than 1 minute. By means of tracer particles it was proven that at this time the fluid in the cell is at rest. The time between consecutive runs is at least 3 minutes to secure independent runs. The influence of the waiting time on the occurring patterns was tested and no effect concerning the wavelength of the fingers was observed.

### 2.2 Experimental results

Fig. 2 shows typical images of the sand-water cell at certain stages. 20 ms after the series of snapshots is started, the initial flat sand layer is modulated at small scales (Fig. 2(a)). These disturbances are enhanced and give rise to sand fingers as seen in Fig. 2(c). At later stages the fingers evolve to a mushroom-like pattern (Fig. 2(d) and Fig. 2(e)). This type of pattern was found also by numerical simulations for two stratified suspensions of different concentration [24].

To analyze this behavior we apply a threshold algorithm to obtain the water-sand interface. We look at every column of our digitized image to determine the point where the grey scale exceeds a certain value. We start at the bottom (water) and continue to the top (sand). In this way we track down the interface of the pattern. Fig. 3 shows the temporal evolution of the images presented in Fig. 2. Here the interfaces of all patterns are shown. While our detecting method works for the patterns during the first stages, namely small scale modulations and sand fingers, it breaks down for mushroom-like patterns. However, this is not crucial because those patterns are beyond the scope of the linear analysis presented here. Discrete-Fourier-Transformation (DFT) gives the Fourier spectrum of each interface. Fig. 4 shows the temporal evolution of the amplitude  $A$  of a typical Fourier mode. It is seen that  $A$  grows exponentially from the first image to  $t = 200$  ms. By an exponential fit

$$A(k) = A_i(k) \exp(n(k)t) \quad (1)$$

we obtain the growth rate  $n$  for every wave number  $k$  in our spectra, where  $A_i$  is the initial amplitude. For each fit it was monitored that  $A(k)$  was smaller than 40 % of its wavelength, the criterion for the linear regime [25].

In order to test the reliability of our experimental setup we perform 100 independent runs with one set of material parameters. The particular values of this set are given in the first row of Table I (Experiment I). We only analyze image series where the angular velocity of our rotating apparatus is larger than 6.6 rad/s. We find that 42 fast runs show only a slight deviation in the angular velocity:  $7.4 \pm 0.1$  rad/s. These 42 measurements are analyzed to obtain

a mean growth rate and a mean initial amplitude for each wave number. The results are shown in Fig. 5. It is seen that the growth rates starting with small values increase with increasing wave number until they saturate at larger  $k$ . In contrast the initial amplitude decreases for increasing wave numbers. In the case of large wave numbers we do not obtain *exponential* fits for every experimental run. This is due to the fact that the amplitude is very small and that we approach the limit of the resolution of our image processing. The error bars in Fig. 5 indicate that the number of runs which can be analyzed decreases for larger wave numbers.

An obvious question concerning the underlying mechanism of the pattern formation in our system is: How do different material parameters effect the dispersion relation? Therefore we carry out experiments with different material configurations which are characterized in Table I. Using 2 g, 4 g, and 8 g of sand (Experiment I, II, III) we observe a shift of all growth rates towards larger values with increasing mass of sand. This effect is independent of the wave number (Fig. 6 (a)). Using three different size distributions (Experiment I, IV, V) the ratio of the cell thickness of 4 mm to the mean particle diameter varies between  $\sim 70$  and  $\sim 40$ . As figure 6 (b) shows the mean particle diameter does not have any significant influence on the dispersion relation  $n(k)$ . As a common feature we find the same overall behavior for all material sets: The growth rates increase for small  $k$  and reach a plateau for larger values of  $k$ .

### 3 Theory

We choose a two fluid system as a model to describe the experimental results. In the initial state two incompressible fluids of constant densities  $\rho_1$  and  $\rho_2$  and constant dynamical viscosities  $\mu_1$  and  $\mu_2$  are arranged in two horizontal strata. The index 1 (2) refers to the fluid at the bottom (top) of the system. The pressure is a function of the vertical coordinate  $z$  only;  $x$  and  $y$  are the coordinates in the plane perpendicular to  $z$ . The acceleration due to gravity acts in negative  $z$  direction. A *linear* stability analysis is carried out for small disturbances of this initial state. The instability of a planar interface  $z = z_s(x, y) \equiv 0$  between the two fluids is known as the Rayleigh-Taylor instability [25, 26, 27].

We assume that the boundaries in  $z$  direction are far from the interface. Small changes  $\delta z_s$  in the form of the interface cause a pressure difference which is balanced by the product of the surface tension  $T_s$  and the curvature of the interface. Considering small disturbances  $\delta\rho$  in the density and  $\delta p$  in the pressure the Navier-Stokes equations read [27]

$$\rho\partial_t u = -\partial_x\delta p + \mu\Delta u + (\partial_x w + \partial_z u)\partial_z\mu \quad , \quad (2)$$

$$\rho\partial_t v = -\partial_y\delta p + \mu\Delta v + (\partial_y w + \partial_z v)\partial_z\mu \quad , \quad (3)$$

$$\rho\partial_t w = -\partial_z\delta p + \mu\Delta w + 2\partial_z w\partial_z\mu - g\delta\rho + T_s(\partial_x^2 + \partial_y^2)\delta z_s\delta(z - z_s) \quad , \quad (4)$$

where  $\partial_i = \partial/\partial i$ ,  $i = x, y, z, t$ . The  $z$  dependence of  $\mu$  gives rise to the third term at the right-hand side of (2-4) since the viscous part in the Navier-Stokes equations is  $\partial_j[\mu(\partial_j v_i + \partial_i v_j)]$  for an incompressible fluid. For convenience, we adhere to  $\partial_z\mu$  though  $\partial_z\mu$  is different from zero only at the interface. The components of the velocity field  $\mathbf{v}$  are  $v_x = u$ ,  $v_y = v$ , and  $v_z = w$  and are considered small, so that Eqs. (2-4) contain only terms which are linear in the disturbances. The delta-function  $\delta(z - z_s)$  ensures that the surface tension appears at the interface  $z_s$  between the two fluids. The equation of continuity (mass conservation) for an incompressible fluid is

$$\text{div } \mathbf{v} = \partial_x u + \partial_y v + \partial_z w = 0 \quad . \quad (5)$$

Additionally the equation

$$\partial_t \delta\rho = -(\mathbf{v}\text{grad})\rho = -w\partial_z\rho \quad (6)$$

relates the temporal variations in the density fluctuations to the density jump at the interface which moves with  $w$  in  $z$  direction. The Eqs. (2-6) govern the linearized system. The disturbances are analyzed into *normal modes* thus seeking solutions which  $x$  and  $t$  dependence is proportional to  $\exp(ikx + nt)$ . The wave number is denoted by  $k$  and  $n(k)$  is the growth rate of the corresponding mode  $k$ . If the fluid is confined between two rigid planes the boundary conditions are

$$w = \partial_z w = 0 \quad \text{at } z = \pm\infty \quad . \quad (7)$$

where we shift the planes to infinity for the sake of simplicity. The other boundary conditions are related to the interface. All three components of the velocity and the tangential viscous stresses must be continuous. Using the exponential ansatz for the continuous velocity components, Eq. (5) gives the continuity of  $\partial_z w$ , too. The continuity of  $\mu(\partial_z^2 + k^2)w$  is the condition which ensures that the two tangential stress components are continuous across the interface. Inserting the exponential ansatz into (2-6) and determining the solution of  $w$  in each region in such a way that the boundary condition (7) as well as the interfacial conditions are satisfied leads to the dispersion relation [27]

$$\begin{aligned} & -\left\{ \frac{gk}{n^2} \left[ (\alpha_1 - \alpha_2) + \frac{k^2 T}{g(\rho_1 + \rho_2)} \right] + 1 \right\} (\alpha_2 q_1 + \alpha_1 q_2 - k) \\ & - 4k\alpha_1\alpha_2 + \frac{4k^2}{n} (\alpha_1\nu_1 - \alpha_2\nu_2) [\alpha_2 q_1 - \alpha_1 q_2 + k(\alpha_1 - \\ & - \alpha_2)] + \frac{4k^3}{n^2} (\alpha_1\nu_1 - \alpha_2\nu_2)^2 (q_1 - k)(q_2 - k) = 0. \end{aligned} \quad (8)$$

The abbreviations  $\alpha_{1,2} = \rho_{1,2}/(\rho_1 + \rho_2)$  and  $q_{1,2}^2 = k^2 + n/\nu_{1,2}$  were introduced where  $\nu_{1,2} = \mu_{1,2}/\rho_{1,2}$  is the kinematic viscosity for each region. For the rest of the paper we will use a dimensionless surface tension  $S = T/[(\rho_1 + \rho_2)(g\nu_1^4)^{1/3}]$  if not stated otherwise.

We now briefly discuss the general results of the dispersion relation (8). The configuration where the lighter fluid is on top of the heavier one,  $\rho_2 < \rho_1$ , is always stable,

i.e.,  $\text{Re}\{n(k)\} \leq 0$  for all  $k$ . This is independent of whether there is any surface tension (Fig. 7 (b)) or not (Fig. 7 (a)). If the strata are in the opposite order,  $\rho_2 > \rho_1$ , then the surface tension plays a crucial role. In the case of no surface tension (Fig. 8 (a)) the system is unstable against disturbances of any wave number, i.e.,  $\text{Re}\{n(k)\} \geq 0$  for all  $k$ . If there is a surface tension a critical wave number exists

$$k_c = \sqrt{\frac{g}{T}(\rho_2 - \rho_1)} \quad , \quad (9)$$

and the system is stable (unstable) against modes with wave numbers which are larger (smaller) than  $k_c$  (Fig. 8 (b)). A moderate variation in the relation between the two viscosities  $\nu_1$  and  $\nu_2$  has no strong influence on the general behavior of the growth rates (see Figs. 7 and 8).

The experiments are carried out in a finite-size cell in contrast to our simplification of infinite length in  $z$  direction. We determine now the limits to which this simplification is justified (see also [28]). If the walls of the cell are at  $z = \pm L_z$  the appropriate ansatz for  $w$  is

$$w_1 = a_1 e^{+kz} + a_2 e^{-kz} + b_1 e^{+q_1 z} + b_2 e^{-q_1 z} \quad \text{for } z \leq 0, \quad (10)$$

$$w_2 = c_1 e^{+kz} + c_2 e^{-kz} + d_1 e^{+q_1 z} + d_2 e^{-q_1 z} \quad \text{for } z \geq 0. \quad (11)$$

With the boundary condition  $w = \partial_z w = 0$  at  $z = \pm L_z$  and the analysis at the interface as above one ends up with a system of eight equations for the constants in (10-11). The coefficients of the corresponding matrix are given in the Appendix. The vanishing determinant leads to the dispersion relation  $n(k)$ , its numerical solution is shown in Fig. 9 for different lengths  $L_z$ . The comparison with the data for infinite  $L_z$  shows that there is no real difference as long as  $|L_z| > 3$  mm for the used material parameters. Since the thickness of the sand layer is below this margin we expect finite-size effects. In the case of asymmetrically arranged walls at  $z = -L_1$  and  $z = +L_2$  the dispersion relation shows up to a ratio of  $|L_1|/L_2 \simeq 17$  only a very weak deviation from the results for symmetrical walls.

In the frame of our continuum approach we consider the water-sand mixture as a suspension in accordance with the classification in [29]. The dispersion medium is water and the dispersed material consists of sand particles with a mean diameter and a density as stated in Sect. 2. The material density as well as the dynamical viscosity of the mixture depend on the packing density  $\phi$  of the granular material. The packing density  $\phi$  measures the volumetric concentration of the particles in the mixture. The material density of the mixture is given by

$$\rho_{mixture} = \phi \rho_{sand} + (1 - \phi) \rho_{water} \quad . \quad (12)$$

Since  $\rho_{water}$  and  $\rho_{sand}$  are constant, the considered small disturbances in the mixture density  $\delta \rho_{mixture}$  imply that  $\phi$  varies according to Eq. (12). In the following the index 1 refers to water and 2 to the mixture, respectively. Two empirical formulae [30,31]

$$\frac{\mu_2}{\mu_1} = \mu_r = \left(1 - \frac{\phi}{\phi_{max}}\right)^{-2.5\phi_{max}} \quad \phi_{max} = 0.63, \quad (13)$$

$$\frac{\mu_2}{\mu_1} = \mu_r = \left(1 + \frac{0.75}{\frac{\phi_{max}}{\phi} - 1}\right)^2 \quad \phi_{max} = 0.605, \quad (14)$$

were widely used for the dynamical viscosity of a hard sphere suspension. The maximal packing densities in (13, 14) result from the fit of the proposed formulae to the experimental results.

Figure 10 shows the behavior of the relative dynamical viscosity  $\mu_r$  for different packing densities  $\phi$  according to Eqs. (13, 14). A third relation,  $\mu_r \simeq 1/[1 - (\phi/\phi_{max})]^{1/3}$  with  $\phi_{max} = 0.625$ , was also plotted where particle sizes beyond the colloidal range were incorporated into the theoretical basis of this relation [32]. All three of them give nearly the same value for  $\mu_r(\phi)$  at moderately dense packings,  $0.4 \leq \phi \leq 0.48$ . Above this region the relative viscosity diverges as  $\phi$  approaches its maximal value. But the strength of the divergent behavior is remarkably different so that  $\mu_r$  already varies about a factor of 5 for  $\phi = 0.57$ . The fact of wide spread measured values for the relative viscosity of the same system is exemplarily shown in [33]. The measured values of  $\mu_r$  vary between 21 and 400 for a rather colloid system at  $\phi \approx 0.5$ . A similar situation is present for suspensions [34] which is why we cannot rely on a fixed value of  $\mu_r$  within small error bars. Therefore we consider  $\mu_r$  a variable parameter within reasonable limits rather than a fixed material parameter.

## 4 Results and Discussion

In experiment I the height of the sedimented sand layer was measured by an optical close-up with a resolution of  $37 \mu\text{m}$  per pixel. On the basis of six independent samples the height was determined to  $2.6 \pm 0.2$  mm. This results in a packing density of  $\phi = 0.48 \pm 0.04$ . Thus the mixture is sufficiently characterized by Eqs. (12-14) where  $\rho_{water} = 0.988 \text{ g/cm}^3$ . By means of (14) the viscosity of the mixture is  $\mu_2 \simeq 15\mu_1$  for  $\phi = 0.48$ . The resulting growth rates show disagreement for infinite  $L_z$  as well as for finite  $L_z$  (Fig. 11). Since the relative dynamical viscosity is the most uncertain quantity in our calculations we vary  $\mu_r$  to find the best fit with the experimental data. Under the assumption of zero surface tension a least square fit results in  $\mu_2 \simeq 104 \mu_1$  which gives a fairly good agreement over the whole  $k$  range. In comparison to  $\mu_2 \simeq 104 \mu_1$ , fits with  $\mu_2 \simeq 128 \mu_1$  and  $\mu_2 \simeq 85 \mu_1$  show a better agreement for smaller and larger wave numbers  $k$ , respectively.

For two sets of parameters,  $\mu_2 \simeq 15 \mu_1$  and  $\mu_2 \simeq 104 \mu_1$ , we calculate the dispersion relation for infinite as well as for finite  $L_z$ . The finite-size effects appear for small wave numbers and decrease with increasing wave numbers. The differences in  $n(k)$  for small wave numbers are more pronounced for larger relative viscosities (see Fig. 11). The dispersion relations for infinite and finite  $L_z$  approach each other at wave numbers where the initial amplitudes of the disturbances are in the order of  $10^{-2}$  mm. For these disturbances a boundary at 2.6 mm distance appears to be at infinity. Therefore it does not matter whether we choose  $L_z = \pm\infty$  or  $L_z = \pm 2.6$  mm. This is not the case for

small wave numbers where the initial amplitudes are in the order of  $10^{-1}$  mm (Fig. 5 (b)).

There is one viscosity measurement [35] which comes near to the value of the relative viscosity suggested by our fit. The measurement was carried out for crushed sand with particle diameters from 20 to 80  $\mu\text{m}$  and gives a value of  $\mu_2 \sim 110 \mu_1$  for  $\phi = 0.48$  (see Fig. 3 in [35]). This value for the relative viscosity is notably close to our fit value. The values for the viscosity of the suspension estimated in [19],  $\mu_2 \sim (130 - 190) \mu_1$ , are in a similar range as ours. These values are determined by the help of the *singular* wave number with the largest growth rate. A real comparison with our fit value is not possible because the necessary packing density is not given for the type of experiments from which the viscosity values were estimated.

Nevertheless, the large difference in  $\mu_r$  between [30, 31, 32] and [35] over a wide range of the packing density  $\phi$  represents an unsatisfying situation. It highlights the need for comprehensive and unambiguous viscosity measurements in highly concentrated hard sphere suspensions. It further shows how sensitive  $\mu_r$  is on experimental methods [32], the accurate determination of the density packing [33], and the type of flow involved in the measurements [36].

The aspect ratio of the cell suggests that a description referring to the Hele-Shaw type of the cell might be closer to the experimental configuration. Adapting the dispersion relation of the Saffman-Taylor instability to the case of zero throughflow velocity leads to [37]

$$n(k) = \frac{b^2}{12(\mu_1 + \mu_2)} [kg(\rho_2 - \rho_1) - Tk^3] \quad (15)$$

where  $b = 4$  mm denotes the width of the cell. In contrast to the Rayleigh-Taylor approach Eq. (15) contains two parameters, the dynamical viscosity  $\mu_2$  of the mixture and the surface tension  $T$ , which have to be determined by a least square fit. The validity of the Hele-Shaw approach is limited by a cut-off condition at which the wave number exceeds  $2\pi/b$ .

The fit values  $\mu_2 \simeq 404 \mu_1$  and  $T \simeq 1.06 \cdot 10^{-3} \text{ Nm}^{-1}$  result in a fit curve which is inferior to the Rayleigh-Taylor fit (Fig. 12). Additionally, both fit parameters are questionable. The value  $\mu_2 \simeq 404 \mu_1$  is beyond any realistic one for the dynamical viscosity of the mixture at a packing density of  $\phi = 0.48$ . A nonzero surface tension between the water-sand mixture and water is also arguable.

The better agreement of the Rayleigh-Taylor approach with the experimental data is backed up by calculations focused on the influence of finite cell boundaries for Rayleigh-Bénard convection [38]. As long as the ratio between the relevant height of the cell and its width is smaller than 0.8, the assumption of infinite boundaries in  $y$  direction is a good approximation. If this ratio is larger than 5 the Hele-Shaw approach is well-founded. The height of the sand layer and the width of the cell give a ratio of 0.65 which supports the Rayleigh-Taylor approach. As a consequence the cell width has no influence on the instability for the used material sets.

It has to be stressed that both the Hele-Shaw and the Rayleigh-Taylor approach assume a trivial  $y$  dependence

of the flow. In the experiment, that assumption is not totally fulfilled: The rotation of the apparatus leads to a sand layer which is not perfectly flat even in the beginning of the flow process. This will lead to a three-dimensional flow which effects the appearing patterns and their wavelengths. The strength of this effect is, however, presently hard to determine.

## 5 Concluding Remarks

In a closed Hele-Shaw-like cell the temporal evolution of a water-sand interface was investigated. For the unstable stratification, sand above water, the instability is driven by gravity. The images of the temporal evolution were analyzed by DFT. The Fourier spectra show that the initial disturbances of the interface grow exponentially at the beginning of the pattern forming process. This enables us to determine the growth rates by an exponential fit for every wave number in our spectra. The data show that the growth rate increases with increasing wave number until it saturates at larger values of  $k$ . This general behavior is not influenced by the mean particle diameter which was tested with three different size distributions. Experiments with different amounts of sand reveal a shift of the dispersion relation  $n(k)$  as a whole. By increasing the mass of sand,  $n(k)$  is shifted towards larger values of  $n$ .

To describe the general behavior we choose a two-fluid system as a model. Carrying out a linear stability analysis for the interface between the two fluids we calculate the growth rates from the dispersion relation for a finite-size cell. The theoretical results agree with the essence in the experimental findings when assuming a relative viscosity of the water-sand mixture which is close to one measured with crushed sand and water [35].

Considering our simplifications and the uncertainty in one relevant material parameter, the continuum approach gives a reasonable agreement with the experimental results. An interpretation for such an agreement was proposed in [19]. Above a critical value of the packing density the mixture exhibits a non-zero yield stress well known for dry granular material. Below this critical value the yield stress vanishes and the mixture behaves more like a fluid with effective properties. Applying this interpretation, the measured packing density of  $\phi = 0.48$  is below this critical value. Thus, our results confirm a certain analogy between concentrated suspensions and fluids which was found also in numerical simulations [24]. However, further investigations need to be done in order to clarify open questions.

The available experimental data give no hint on whether the dispersion relation  $n(k)$  will have a second zero at  $k_c$  after the observed plateau. A critical wave number  $k_c$  means a non-zero interfacial tension according to (9). A surface tension acts in a way to minimize the surface of the fluid. Therefore it suppresses the formation of waves with large wave numbers because their creation entail additional surface. The suppression leads to a saturation (reduction) in the growth rates of disturbances with large (very large) wave numbers. In the context of miscible fluids with slow diffusion the concept of an effective dynamical

ical surface tension was recently successfully applied [39]. The reason for such a surface tension lies in the attraction between moving particles in a fluid for non-zero Reynolds numbers [40]. The attraction originates from the dynamics in the viscous fluid and results in a favoured distance between the moving particles. Consequently, it costs energy to separate the particles beyond this favoured distance, i.e., to dilute the suspension. The necessary energy corresponds to a surface tension which is called effective *dynamical* surface tension to emphasize its dynamical origin. The effect of such an effective dynamical surface tension is seen in experiments by the presence of sharp interfaces in rising bubbles, falling drops [41] and of growing deposits [39]. A concentration gradient concerning sand is present in our system between the water and the water-sand layer. By reducing the density difference between the layers, measurements for  $k$  values beyond the plateau should be possible. This may lead towards the determination of  $k_c$  and the interfacial tension, respectively.

Since a linear stability analysis is restricted to terms linear in the disturbances we cannot take into account fluctuations in the relative viscosity of the mixture. These would lead to terms of higher order because all terms which contain the viscosity are already linear in the velocity disturbances (see 2-4). On the other hand, considering fluctuations of  $\rho_{mixture}(\phi)$ , i.e., fluctuations of the packing density  $\phi$ , implies variations of  $\mu_r(\phi)$ . This inconsistency owing to the restrictions of our linear theory can only be resolved in a nonlinear analysis.

We are grateful to Lluís Carrillo, Stefan Naser, and Stefan Schwarzer for inspiring discussions. The experiments were supported by DFG through Re 588/11-1.

## 6 Appendix

The matrix elements for finite  $L_z$  are  $A_{11} = e^{-kL_z}$ ,  $A_{12} = e^{kL_z}$ ,  $A_{13} = e^{-q_1 L_z}$ ,  $A_{14} = e^{q_1 L_z}$ ,  $A_{15} = A_{16} = A_{17} = A_{18} = 0$ ,  $A_{21} = ke^{-kL_z}$ ,  $A_{22} = -ke^{kL_z}$ ,  $A_{23} = q_1 e^{-q_1 L_z}$ ,  $A_{24} = -q_1 e^{q_1 L_z}$ ,  $A_{25} = A_{26} = A_{27} = A_{28} = A_{31} = A_{32} = A_{33} = A_{34} = 0$ ,  $A_{35} = e^{kL_z}$ ,  $A_{36} = e^{-kL_z}$ ,  $A_{37} = e^{q_2 L_z}$ ,  $A_{38} = e^{-q_2 L_z}$ ,  $A_{41} = A_{42} = A_{43} = A_{44} = 0$ ,  $A_{45} = ke^{kL_z}$ ,  $A_{46} = -ke^{-kL_z}$ ,  $A_{47} = q_2 e^{q_2 L_z}$ ,  $A_{48} = -q_2 e^{-q_2 L_z}$ ,  $A_{51} = A_{52} = A_{53} = A_{54} = 1$ ,  $A_{55} = A_{56} = A_{57} = A_{58} = -1$ ,  $A_{61} = k$ ,  $A_{62} = -k$ ,  $A_{63} = q_1$ ,  $A_{64} = -q_1$ ,  $A_{65} = -k$ ,  $A_{66} = k$ ,  $A_{67} = -q_2$ ,  $A_{68} = q_2$ ,  $A_{71} = A_{72} = 2\mu_1 k^2$ ,  $A_{73} = A_{74} = \mu_1 (q_1^2 + k^2)$ ,  $A_{75} = A_{76} = -2\mu_2 k^2$ ,  $A_{77} = A_{78} = -\mu_2 (q_1^2 + k^2)$ ,  $A_{81} = R/2 - C - \alpha_1$ ,  $A_{82} = R/2 + C + \alpha_1$ ,  $A_{83} = R/2 - q_1 C/k$ ,  $A_{84} = R/2 + q_1 C/k$ ,  $A_{85} = R/2 - C + \alpha_2$ ,  $A_{86} = R/2 + C - \alpha_2$ ,  $A_{87} = R/2 - q_2 C/k$ , and  $A_{88} = R/2 + q_2 C/k$ . Furthermore, the abbreviations

$$R = \frac{k}{n^2} \left[ g(\alpha_2 - \alpha_1) + \frac{k^2 T}{\rho_1 + \rho_2} \right] \quad \text{and} \quad (16)$$

$$C = \frac{k^2}{n} (\alpha_1 \nu_1 - \alpha_2 \nu_2) \quad (17)$$

were used.

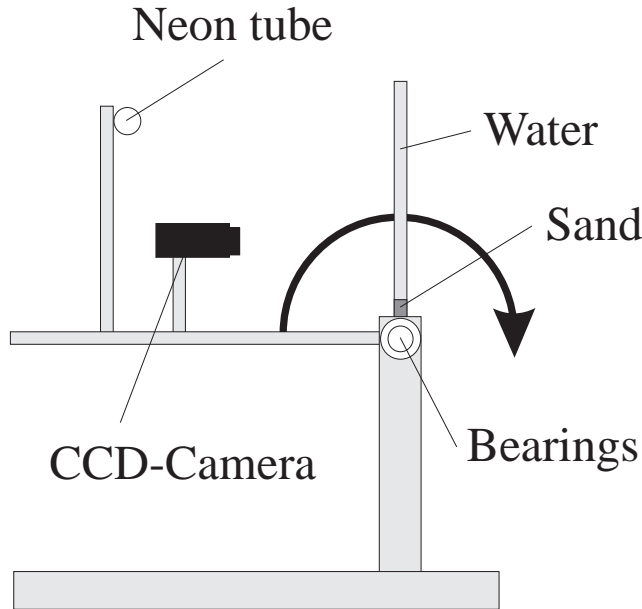
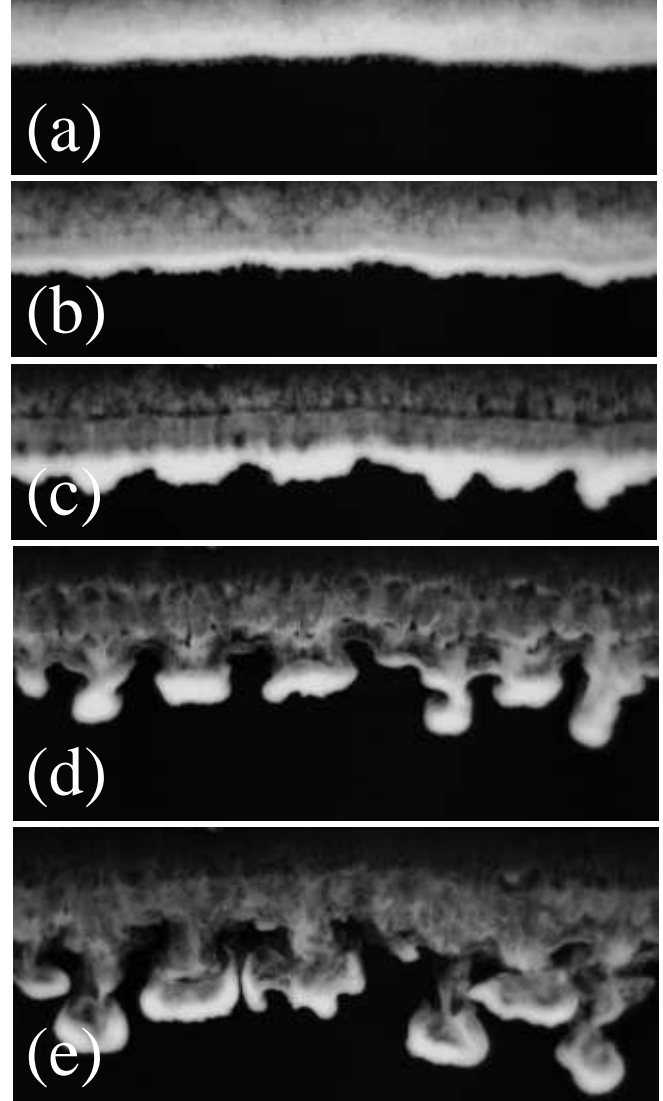
## References

1. H.M. Jaeger, S.R. Nagel, R.P. Behringer, *Rev. Mod. Phys.* **68**, 1259 (1996).
2. P.B. Umbanhowar, F. Melo, H.L. Swinney, *Nature* **382**, 793 (1996).
3. H.A. Makse, S. Havlin, P.R. King, H.E. Stanley, *Nature* **386**, 379 (1997).
4. D.E. Goldsack, M.F. Leach, C. Kilkenny, *Nature* **386**, 29 (1997).
5. G.H. Ristow, in *Annual Reviews of Computational Physics*, Vol. I, edited by D. Stauffer (World Scientific, Singapore, 1994), p. 275.
6. V. Buchholtz, T. Pöschel, H.-J. Tillemans, *Physica A* **216**, 199 (1995).
7. G.A. Kohring, *J. Phys. I (France)* **5**, 1551 (1995).
8. P.K. Haff, *J. Fluid Mech.* **134**, 401 (1983); J.T. Jenkins, M.W. Richman, *J. Fluid Mech.* **192**, 313 (1988).
9. J.T. Jenkins, S.B. Savage, *J. Fluid Mech.* **130**, 187 (1983); J.T. Jenkins, *J. Appl. Mech.* **59**, 120 (1992).
10. H. Hayakawa, S. Yue, D.C. Hong, *Phys. Rev. Lett.* **75**, 2328 (1995).
11. E.L. Grossman, T. Zhou, E. Ben-Naim, *Phys. Rev. E* **55**, 4200 (1997).
12. O. Pouliquen, J. Delour, S.B. Savage, *Nature* **386**, 816 (1997); O. Pouliquen, S.B. Savage, Fingering instability in granular chute flows, preprint (1996).
13. H.E. Huppert, *Nature* **300**, 427 (1982).
14. F. Melo, P. Umbanhowar, H.L. Swinney, *Phys. Rev. Lett.* **72**, 172 (1994).
15. S. Fauve, K. Kumar, C. Laroche, D. Beysens, Y. Garrabos, *Phys. Rev. Lett.* **68**, 3160 (1992).
16. R.A. Bagnold, *Proc. R. Soc. London A* **225**, 49 (1954); **295**, 219 (1966).
17. M. Schröter, Diploma thesis, University of Magdeburg, 1997.
18. A.T. Skjeltorp, in *Time-Dependent Effects in Disordered Materials*, edited by R. Pynn, T. Riste (Plenum Press Corporation, New York, 1987), p. 71.
19. A.K. Didwania, G.M. Homsy, *Ind. Eng. Chem. Fundam.* **20**, 318 (1981). We are referring especially to the experimental runs where an initially unsaturated bed of beads was suddenly exposed to a high velocity fluid.
20. K. Zhang, A. Acrivos, U. Schafinger, *Int. J. Multiphase Flow* **18**, 51, (1992).
21. I. Rubinstein, *Int. J. Multiphase Flow* **6**, 473 (1980).
22. W.-F. Leung, R.F. Probstein, *Ind. Eng. Chem. Process Des. Dev.* **22**, 58 (1983).
23. G. Amberg, A.A. Dahlkild, *J. Fluid Mech.* **185**, 415 (1987).
24. O.A. Druzhinin, *Phys. Fluids* **7**, 315 (1997).
25. D.H. Sharp, *Physica D* **12**, 3 (1984).
26. Lord Rayleigh, *Proc. London Math. Soc.* **14**, 170 (1883); G. Taylor, *Proc. R. Soc. London A* **201**, 192 (1950); D.J. Lewis, *Proc. R. Soc. London A* **202**, 81 (1950).
27. S. Chandrasekhar, *Hydrodynamic and Hydromagnetic Stability* (Oxford University Press, Oxford, 1961), Chapt. X.
28. K.O. Mikaelian, *Phys. Rev. E* **54**, 3676 (1996).
29. H. Rumpf, *Particle Technology* (Chapman and Hall, London, 1990), p. 8.
30. I.M. Krieger, T. J. Dougherty, *Trans. Soc. Rheol.* **3**, 137 (1959).
31. J.S. Chong, E.B. Christiansen, A.D. Baer, *J. Appl. Polym. Sci.* **15**, 2007 (1971).

**Table 1.** Details of sand used in certain experimental configurations.

Experiment	Size distribution [ $\mu\text{m}$ ]	Mass [g]	Runs
I	71-80	2	100
II	71-80	4	12
III	71-80	8	12
IV	56-63	2	12
V	90-100	2	12

32. N.A. Frankel, A. Acrivos, *Chem. Eng. Sci.* **22**, 169 (1967); A. Acrivos in *Particulate Two-Phase Flow*, edited by M.C. Rocco (Butterworth-Heinemann, Boston, 1993), p. 169.
33. S.P. Meeker, W.C.K. Poon, P.N. Pusey, *Phys. Rev. E* **55**, 5718 (1997).
34. M. Ungarish, *Hydrodynamics of Suspensions* (Springer-Verlag, Berlin, 1993), p. 17.
35. L. Arnaud, C. Boutin, in *Theoretical and Applied Rheology*, edited by P. Moldenaers, R. Keunings (Elsevier, Amsterdam, 1992), p. 640.
36. R. Pätzold, *Rheol. Acta* **19**, 322 (1980).
37. P.G. Saffman, G. Taylor, *Proc. R. Soc. London A* **245**, 312 (1958); K.V. McCloud, J.V. Mahler, *Phys. Rep.* **260**, 139 (1995).
38. H. Frick, R.M. Clever, *ZAMP* **31**, 502 (1980).
39. M.-Q. López-Salvans, P.P. Trigueros, S. Vallmitjana, J. Claret, F. Sagués, *Phys. Rev. Lett.* **76**, 4062 (1996).
40. K.O.L.F. Jayaweera, B.J. Mason, G.W. Slack, *J. Fluid Mech.* **20**, 121 (1964).
41. D.D. Joseph, Y.Y. Renardy, *Fundamentals of Two-Fluid Dynamics* (Springer Verlag, New York, 1993), Chapt. X.

**Fig. 1.** Experimental setup.**Fig. 2.** Sand-water interfaces at certain time steps: (a) 20 ms, (b) 80 ms, (c) 140 ms, (d) 200 ms, and (e) 260 ms. The size distribution of the sand particles is given by 71-80  $\mu\text{m}$  and the sand mass in the cell by 2 g, respectively. The presented frames show the middle part of the cell and have a horizontal length of 68 mm.

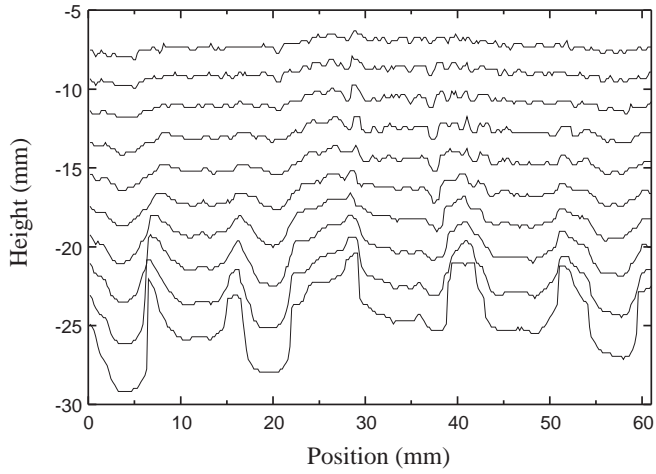


**Fig. 3.** Temporal evolution of the water-sand interfaces. The patterns are detected every 20 ms and shown with a constant vertical offset of 1 mm. The experimental conditions are the same as in Fig. 2.

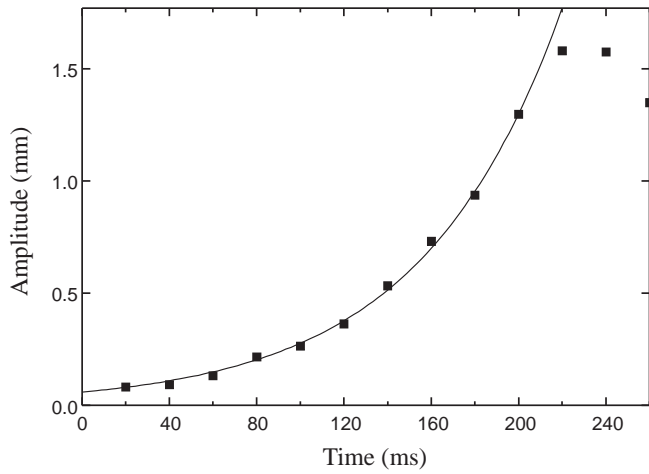


**Fig. 4.** Amplitude  $A$  of a DFT-analysis for a typical wave number (here  $k = 7 \text{ cm}^{-1}$ ) in dependence on time  $t$ . An exponential fit is obtained by Eq. (1). The values belong to the interfaces presented in Fig. 3.

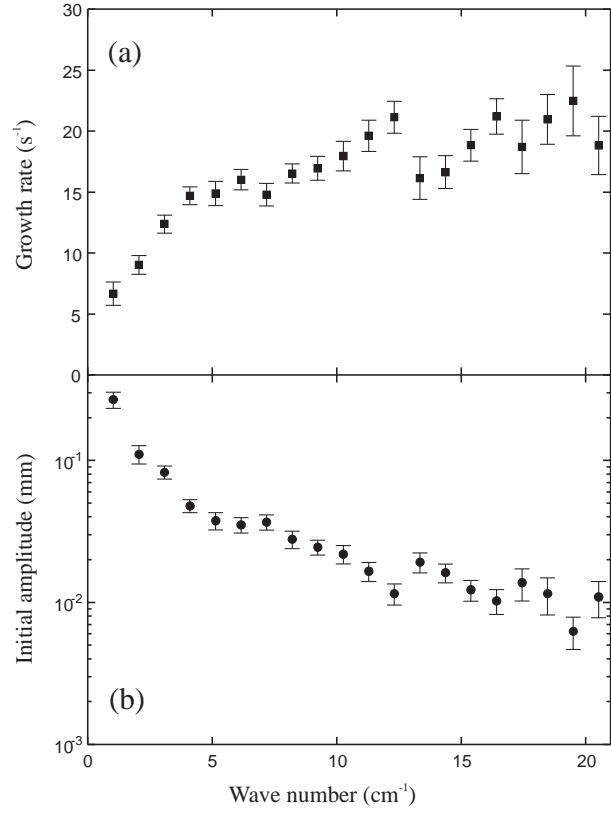


**Fig. 5.** Growth rate (a) and initial amplitude (b) versus the wave number  $k$  for experiment I (see Table 1).

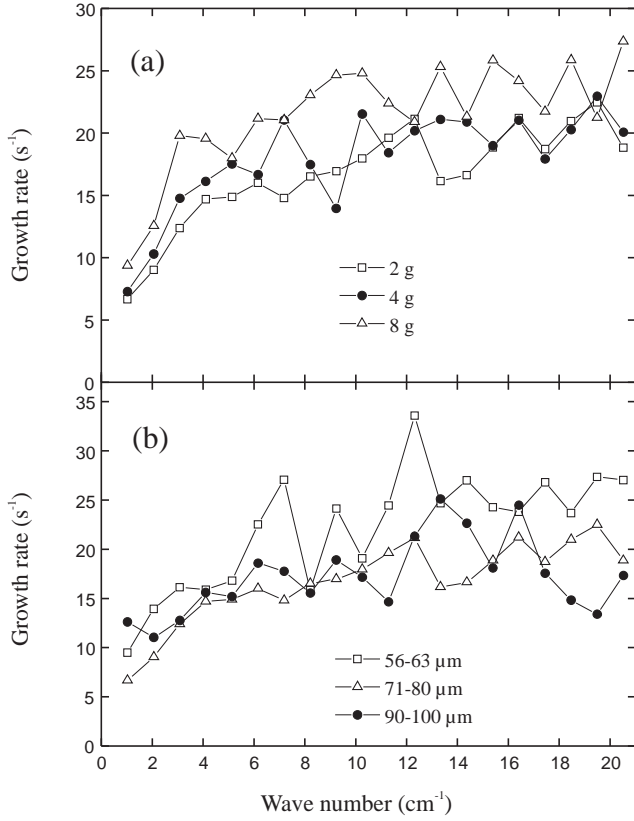


**Fig. 6.** Growth rate versus the wave number for different material parameters. In (a) 2 g ( $\square$ ), 4 g ( $\bullet$ ), and 8 g ( $\triangle$ ) of sand with the same size distribution were used (Experiment I, II, III). In (b) 2 g of sand with size distributions of 56 – 63  $\mu\text{m}$  ( $\square$ ), 71 – 80  $\mu\text{m}$  ( $\triangle$ ), and 90 – 100  $\mu\text{m}$  ( $\bullet$ ) were used (Experiment IV, I, V).

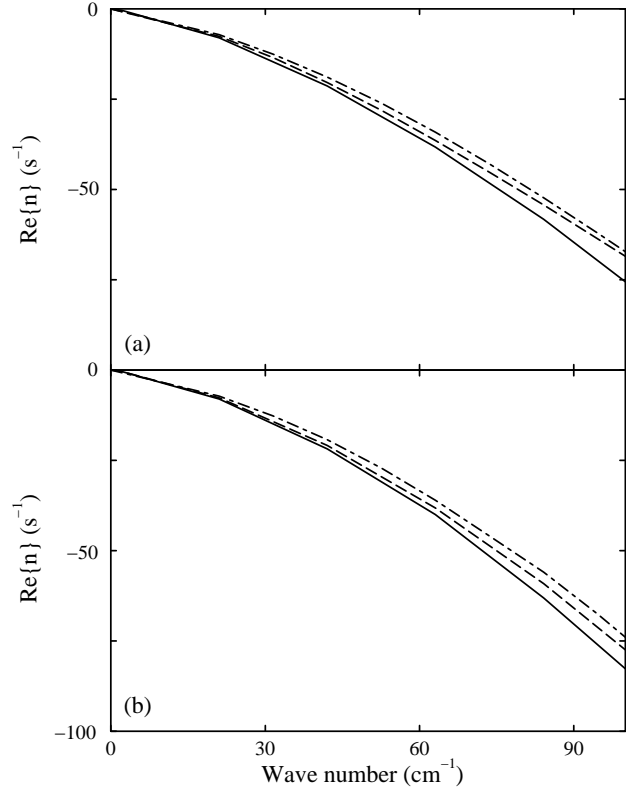


**Fig. 7.** For zero surface tension (a) and surface tension  $S = 1$  (b) the growth rate  $\text{Re}\{n\}$  of the modes is plotted versus their wave number  $k$  for the case that the top fluid is lighter than the bottom one,  $\rho_2 = 0.5\rho_1$ . The surface tension as well as the relation of the viscosities does not change the *overall* behavior too much as the three examples show:  $\nu_1 = \nu_2 = 10^{-6} \text{ m}^2 \text{ s}^{-1}$  (solid line),  $\nu_1 = 10^{-6} \text{ m}^2 \text{ s}^{-1}$  and  $\nu_2 = 0.75\nu_1$  (long-dashed line), and  $\nu_2 = 10^{-6} \text{ m}^2 \text{ s}^{-1}$  and  $\nu_1 = 0.75\nu_2$  (dot-dashed line).

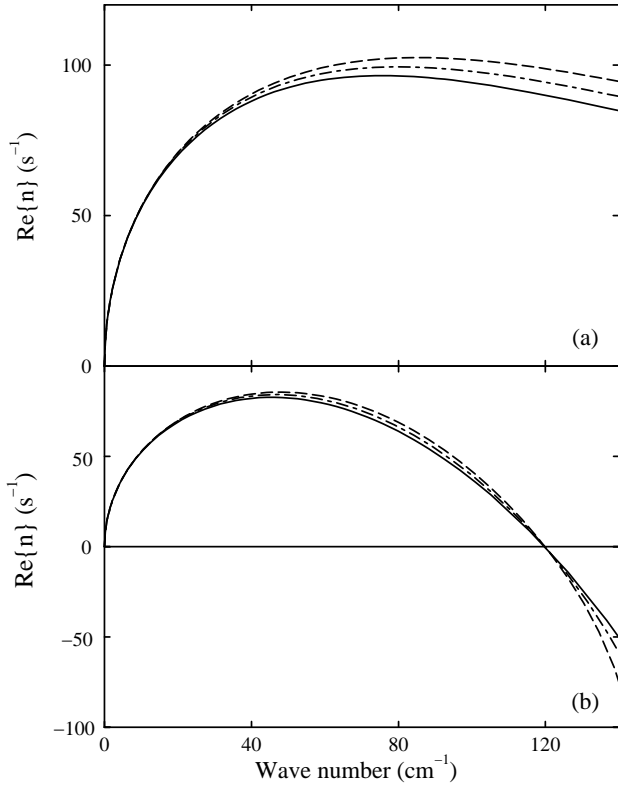


**Fig. 8.** The growth rate  $\text{Re}\{n\}$  of the modes is plotted versus their wave number  $k$  for the case that the top fluid is heavier than the bottom one,  $\rho_2 = 2\rho_1$ . The surface tension  $S$  is zero in (a) and 1 in (b). The surface tension causes a drastic change in the behavior whereas the ratio of the viscosities does not change the *overall* behavior too much as the three examples show:  $\nu_1 = \nu_2 = 10^{-6} \text{ m}^2 \text{ s}^{-1}$  (solid line),  $\nu_1 = 10^{-6} \text{ m}^2 \text{ s}^{-1}$  and  $\nu_2 = 0.75\nu_1$  (long-dashed line), and  $\nu_2 = 10^{-6} \text{ m}^2 \text{ s}^{-1}$  and  $\nu_1 = 0.75\nu_2$  (dot-dashed line).

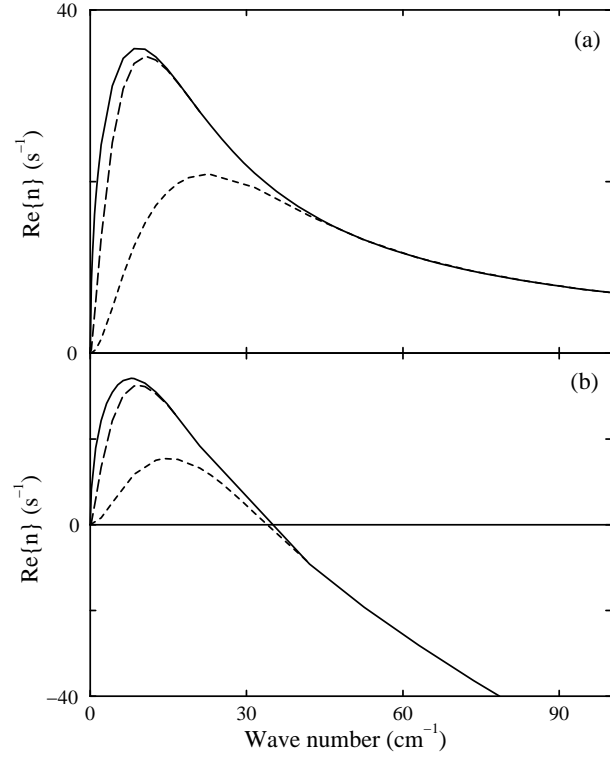


**Fig. 9.** For zero surface tension (a) and surface tension  $S = 12.8$  (b) the growth rate  $\text{Re}\{n\}$  is plotted versus the wave number  $k$  for  $L_z = \pm 3 \text{ mm}$  (long-dashed line) and  $L_z = \pm 1 \text{ mm}$  (dashed line). For comparison the solid line shows the graph for infinite  $L_z$ . It reveals that finite-size effects play a significant role if  $k < 2\pi/|L_z|$ . The material parameters are  $\rho_2 = 2\rho_1$  and  $\nu_2 = 33\nu_1$  with  $\rho_1 = 1 \text{ g cm}^{-3}$  and  $\nu_1 = 10^{-6} \text{ m}^2 \text{ s}^{-1}$ .

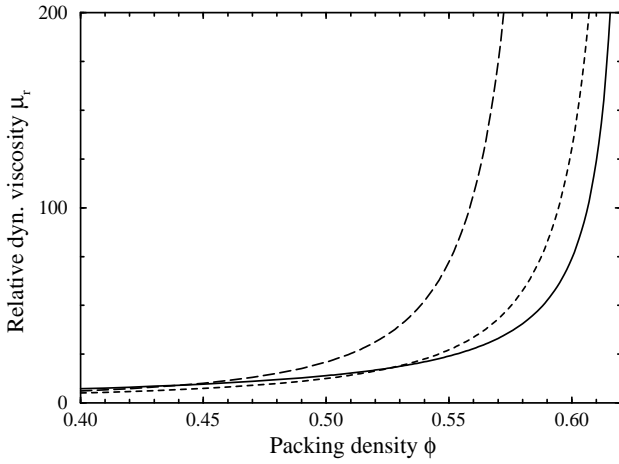


**Fig. 10.** Relative dynamical viscosity  $\mu_r$  versus the packing density  $\phi$ . The results of the two empirical formulae (13, 14) are plotted as dashed and long-dashed lines, respectively. The solid line indicates  $\mu_r \simeq 1/[1 - (\phi/\phi_{max})]^{1/3}$  with  $\phi_{max} = 0.625$  [32].  $\mu_r$  is nearly the same for all three approaches provided the packing is not too dense,  $\phi \leq 0.48$ . Above this range  $\mu_r$  starts to diverge as  $\phi$  reaches  $\phi_{max}$  where the divergent behavior differs significantly between the various approximations.

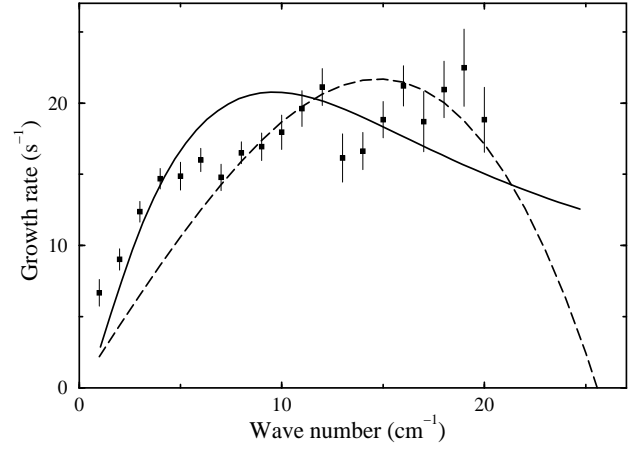


**Fig. 12.** Growth rates  $n$  of the disturbances against their wave numbers  $k$  for a packing density  $\phi = 0.48$ . Two different fits are compared with the experimental results ( $\blacksquare$ ). The solid line shows the graph based on the Rayleigh-Taylor approach with finite  $z$  boundaries at  $|L_z| = \pm 2.6$  mm and  $\mu_r = 104$ . The long-dashed line presents the results of the Hele-Shaw approach with  $\mu_r = 404$  and  $T \simeq 1.06 \cdot 10^{-3}$  Nm $^{-1}$ .

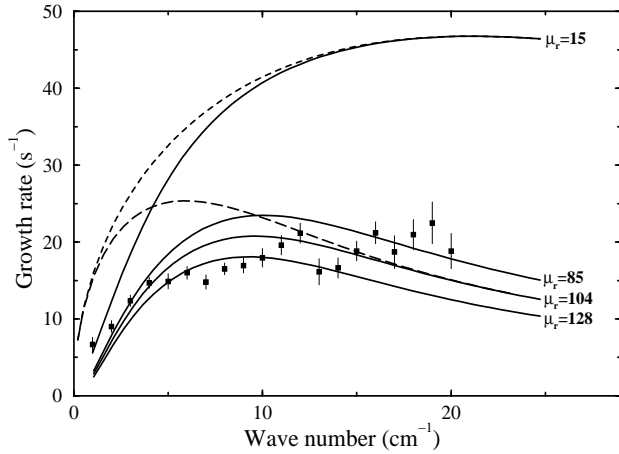


**Fig. 11.** Growth rates  $n$  of the disturbances against their wave numbers  $k$  for a packing density  $\phi = 0.48$ . The results  $n(k)$  for infinite  $L_z$  according to (8) are shown by the dashed line ( $\mu_r = 15$ ) and the long-dashed line ( $\mu_r = 104$ ), respectively. The solid lines are calculated with  $|L_z| = \pm 2.6$  mm, the measured height of the sand layer. The relative viscosity for each drawn curve is stated at the right end of it. The finite-size effects appear for small wave numbers and increase with increasing relative viscosity. A relative viscosity of  $\mu_r = 15$  based on (14) gives growth rates which are far away from the experimental results ( $\blacksquare$ ). The best fit over the whole  $k$  range gives  $\mu_r = 104$ . Fits with slightly smaller or larger  $\mu_r$  values deliver better agreements either with larger or smaller wave numbers.